www.acsnano.org

An Extracellular Vesicle-Cloaked Multifaceted Biocatalyst for Ultrasound-Augmented Tendon Matrix Reconstruction and Immune Microenvironment Regulation

Xiao Rong, Yuanjiao Tang, Sujiao Cao, Sutong Xiao, Haonan Wang, Bihui Zhu, Songya Huang, Mohsen Adeli, Raul D. Rodriguez, Chong Cheng,* Lang Ma,* and Li Qiu*



Downloaded via TOMSK STATE POLYTECH UNIV on September 11, 2023 at 16:22:57 (UTC). See https://pubs.acs.org/sharingguidelines for options on how to legitimately share published articles.

Cite This: https://doi.org/10.1021/acsnano.3c00911



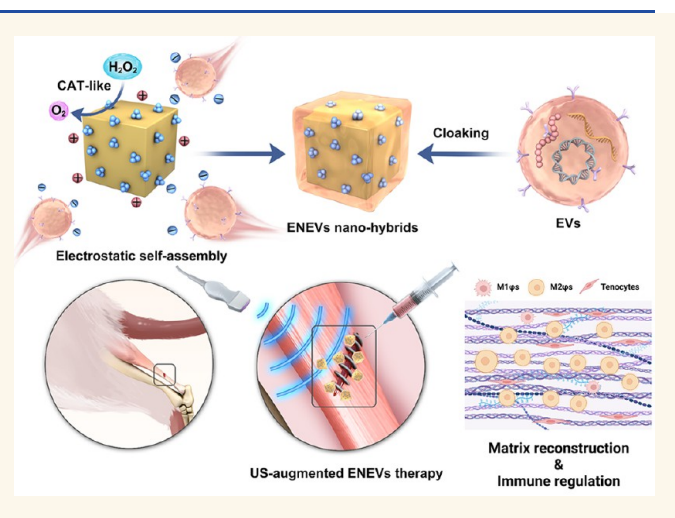
ACCESS

III Metrics & More

Article Recommendations

Supporting Information

ABSTRACT: The healing of tendon injury is often hindered by peritendinous adhesion and poor regeneration caused by the accumulation of reactive oxygen species (ROS), development of inflammatory responses, and the deposition of type-III collagen. Herein, an extracellular vesicles (EVs)-cloaked enzymatic nanohybrid (ENEV) was constructed to serve as a multifaceted biocatalyst for ultrasound (US)-augmented tendon matrix reconstruction and immune microenvironment regulation. The ENEV-based biocatalyst exhibits integrated merits for treating tendon injury, including the efficient catalase-mimetic scavenging of ROS in the injured tissue, sustainable release of Zn²⁺ ions, cellular uptake augmented by US, and immunoregulation induced by EVs. Our study suggests that ENEVs can promote tenocyte proliferation and type-I collagen synthesis at an early stage by protecting tenocytes from ROS attack. The ENEVs also prompted efficient immune regulation, as the polarization of macrophages $(M\varphi)$ was reversed from M1 φ to



 $M2\varphi$. In a rat Achilles tendon defect model, the ENEVs combined with US treatment significantly promoted functional recovery and matrix reconstruction, restored tendon morphology, suppressed intratendinous scarring, and inhibited peritendinous adhesion. Overall, this study offers an efficient nanomedicine for US-augmented tendon regeneration with improved healing outcomes and provides an alternative strategy to design multifaceted artificial biocatalysts for synergetic tissue regenerative therapies.

KEYWORDS: extracellular vesicles, ultrasound, nanomedicines, biocatalytic therapies, anti-inflammatory and tissue regeneration

INTRODUCTION

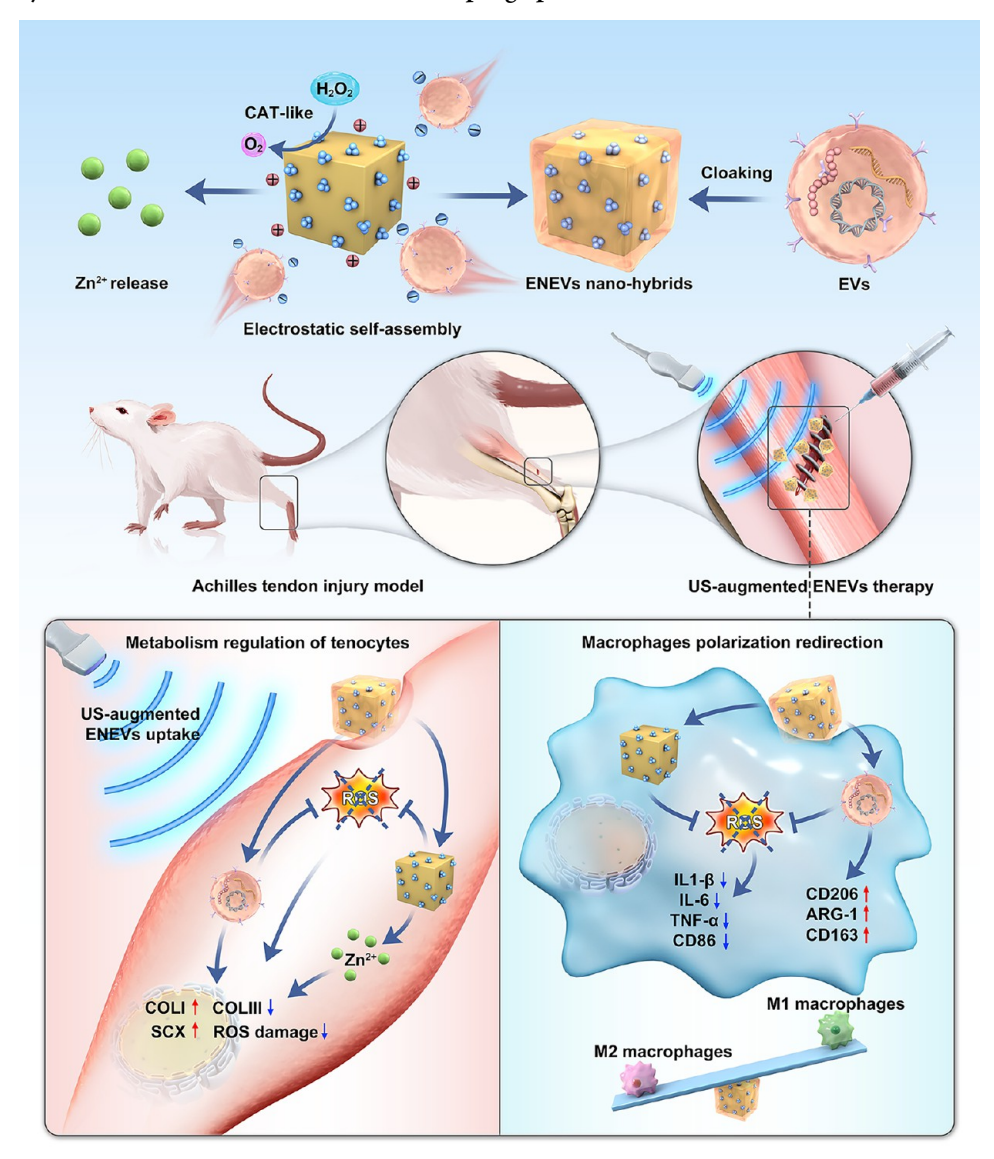
Tendon injury is a common musculoskeletal disorder with increased morbidity due to public engagement in physical exercise. Sustaining tendon injury may severely affect the functions of limbs and result in a poor quality of daily life. Surgical intervention is considered the "gold standard" for acute tendon injury. However, postoperative complications, such as peritendinous adhesion and scar healing, can seriously impair tendon function and are challenging clinical problems without effective prevention strategies to date. Therefore, efficient therapeutic approaches with enhanced tendon regeneration and antiadhesion effects are urgently needed to overcome these clinical bottlenecks.

The healing of tendon injury can be divided into three stages: inflammatory, proliferative, and remodeling. In the initial stage, clinical and experimental studies proved that the level of reactive oxygen species (ROS) constantly increased in acutely injured tendons. The accumulated ROS can result in tenocyte apoptosis, collagen degradation, suppressed tenogenesis, and

Received: January 31, 2023 Accepted: August 17, 2023



Scheme 1. Construction of ENEVs, treatment of rat Achilles tendon injury, and the therapeutic mechanisms involved in the regulation of tenocyte metabolism and redirection of macrophage polarization.



M1 macrophage (M1 φ) polarization. The M1 φ is a main driver of inflammation and the predominant M ϕ phenotype at the onset of tendon injury responsible for secretion of proinflammatory cytokines, including IL-1 β , IL-6, and TNF- α , and further generation of ROS, which exacerbates the inflammatory cycle ¹⁰ and promotes a proinflammatory immune microenvironment. ^{11,12} The proliferative stage is characterized by predominant type-III collagen (COLIII) rather than type-I collagen (COLI) deposition directed by recruited fibroblasts that provide a rapid "patch" to the injured area. 13 Furthermore, the ROS-triggered oxidative stress impairment and inflammation can increase the COLIII/COLI ratio to produce tendon adhesion and fibrosis. 5 COLIII has a smaller diameter and more irregular alignment than that of COLI, which leads to decreased biomechanical strength.¹⁴ Although COLIII could be replaced by COLI in the remodeling stage, 15 this process can take up to 12 months. During this time, the poor mechanical properties of the tendon produce ongoing loss of function and a higher risk of re-rupture. 16 Consequently, it is important to find a comprehensive therapeutic strategy that induces an antiinflammatory response, scavenges ROS, promotes COLI synthesis, and suppresses COLIII deposition to rebuild the tendon matrix and thereby significantly improve tendon injury rehabilitation.

Mesenchymal stem cell (MSC)-derived extracellular vesicles (EVs) are small-sized (50–1000 nm) phospholipid bilayer membranous vesicles that contain protein and nucleic acid released from the host MSCs. The Among them, bone marrow stem cell-derived EVs (BMSC-EVs) have been extensively adopted in musculoskeletal tissue regeneration. Numerous studies have shown that administering BMSC-EVs can promote tendon healing through regulation of the immune microenvironments and improvement of collagen synthesis and tenogenic expression. Although the BMSC-EVs can inhibit the polarization of M1 φ and increase the expression of anti-inflammatory mediators at the early phase of tendon healing, their anti-ROS capacity is very limited and needs to be significantly improved for resolving the accumulation of ROS. Ros. Moreover, the effects of BMSC-EVs on the expression of COLIII vary between studies, and an antiadhesion effect

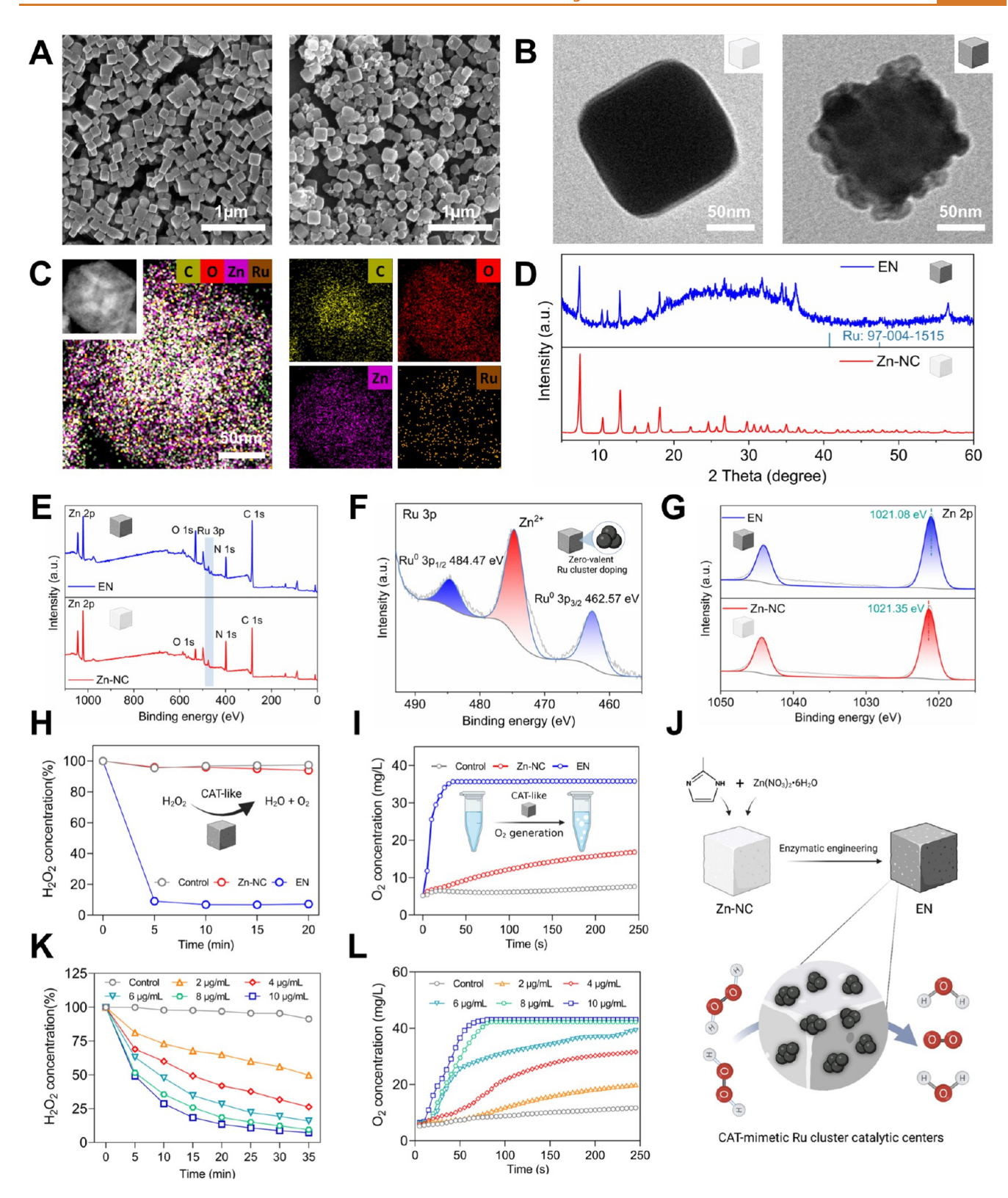


Figure 1. Characterization and ROS-scavenging activity of EN. (A) SEM of Zn-NCs (left) and ENs (right). (B) TEM of Zn-NCs (left) and ENs (right). (C) Elemental mapping of C (yellow), O (red), Zn (purple), and Ru (brown) in ENs. (D) XRD patterns of Zn-NCs and ENs. (E) XPS survey spectra of ENs and Zn-NCs. (F) The Ru 3p XPS analysis of ENs. (G) The Zn 2p XPS analysis of Zn-NCs and ENs. (H) H_2O_2 decomposition and (I) O_2 production properties of Zn-NCs and ENs. (J) Schematic of the construction of ENs and the H_2O_2 -scavenging process. (K) H_2O_2 -scavenging and (L) O_2 generation properties of different concentrations of ENs. In (H) and (K), n=3 per group. In (D), (E), (F), and (G), au indicates arbitrary units. Data are presented as mean \pm SD.

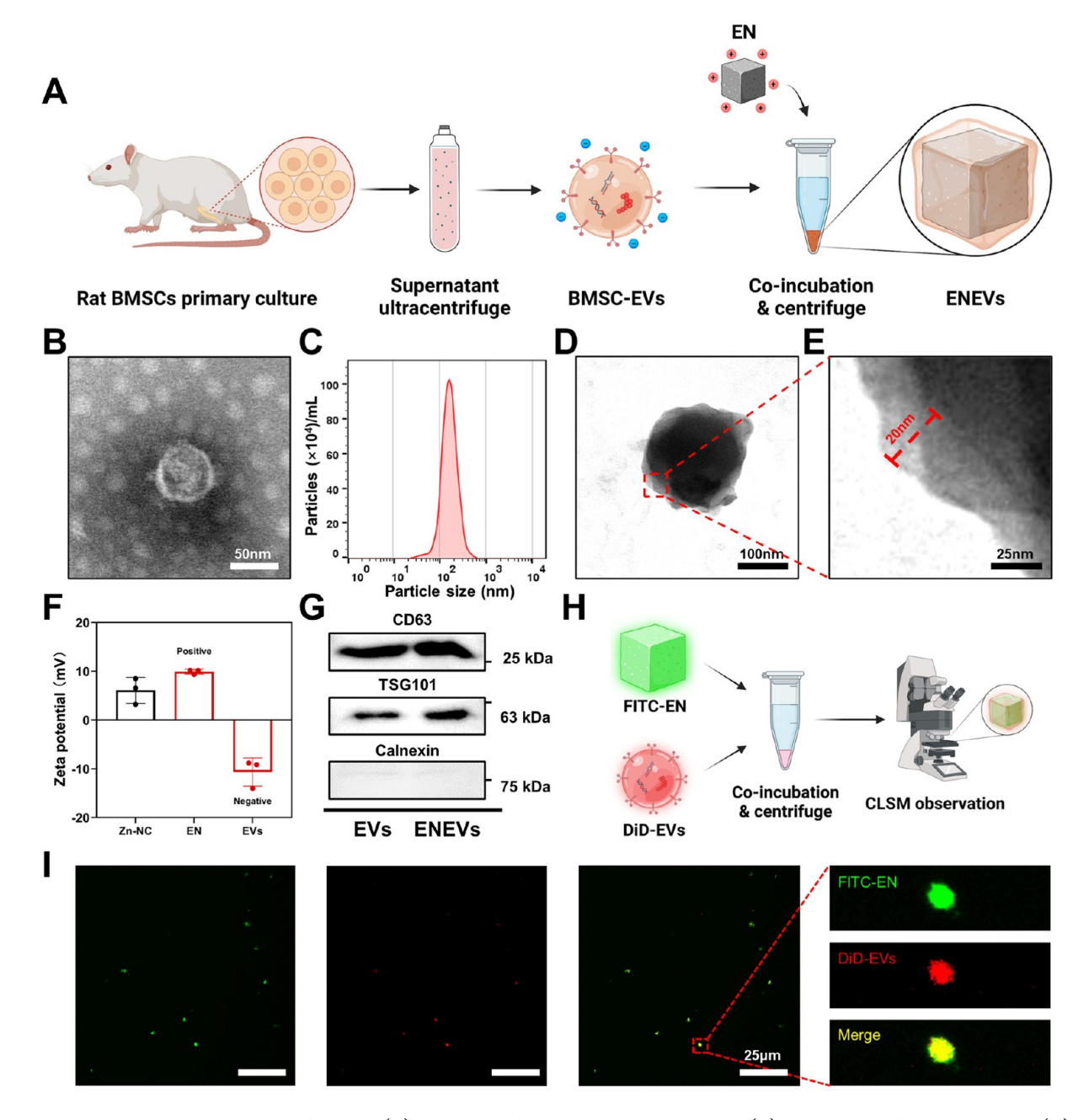


Figure 2. Isolation of EVs and analysis of ENEVs. (A) Schematic of the construction of ENEVs. (B) TEM image of the isolated EVs. (C) NTA result of the size of EVs. (D) TEM image of ENEVs. (E) The magnified edge area of ENEVs; the 20-nm-thick membrane on the surface of ENEVs is marked. (F) Zeta potential was measured with a NanoBrook Omni zeta potential analyzer (n = 3 per group, data are presented as mean \pm SD). (G) Immunoblotting analysis of the EVs markers (CD63 and TSG101) and endoplasmic reticulum marker (calnexin) expressed by EVs or ENEVs. (H) Schematic of the construction of FITC-EN/DiD-EVs for CLSM observation. (I) CLSM images of ENEVs; the green fluorescence is from FITC-labeled EN, and the red fluorescence is from DiD-labeled EVs.

of native BMSC-EVs has yet to be reported. Recent studies revealed that $\mathrm{Zn^{2+}}$ could promote tenocyte accumulation, proliferation, and COLI synthesis but inhibit COLIII deposition, thereby making this an effective component in tendon matrix reconstruction.

To overcome the integrated challenges of excessive ROS, undue inflammatory responses, and insufficient COLI synthesis during tendon injury, we created an EVs-cloaked enzymatic nanohybrid (ENEVs) to act as a multifaceted biocatalyst for ultrasound (US)-augmented tendon matrix reconstruction and immune microenvironment regulation (Scheme 1). Notably, the ENEVs exhibited several integrated advantages for treating

tendon injury, including efficient catalase (CAT)-mimetic scavenging of ROS, sustainable release of Zn²⁺ ions to promote COLI synthesis, and inhibition of COLIII deposition together with cellular uptake augmented by US and immunoregulation induced by EVs. Thus, the ENEVs represent a synergetic regenerative strategy among reported nanomedicine-based tissue-healing therapy. COLI and COLIII syntheses, polarization of macrophages, and tendon recovery were comprehensively explored via cellular studies and the rat Achilles tendon defect model. This study demonstrates that the ENEVs, with US assistance, can significantly restore tendon morphology

ACS Nano www.acsnano.org Article

and function, promote matrix reconstruction, suppress intratendinous scar formation, and inhibit peritendinous adhesion.

RESULTS AND DISCUSSION

Structural Characterization and ROS-Scavenging **Evaluation.** The EVs-cloaked multifaceted biocatalyst was synthesized via a three-step method. First, a uniform Zn-based nanocube (Zn-NC) was obtained by one-pot coordination of Zn²⁺ ions and dimethylimidazole ligands in an aqueous solution (Figure S1). Ruthenium (Ru) catalytic sites, owing to their low electronegativity and higher metal state, exhibit electron enrichment and a greater occupancy of occupied orbitals in oxygen activation reactions and antioxidase-like activities.²⁷ Thus, we chose Ru clusters to construct ENs with antioxidaselike ROS-scavenging ability. The Zn-NCs were homodispersed in a RuCl₃ aqueous solution to form the Ru-doped Zn-NCs; thereafter, NaBH was added dropwise to reduce Ru³⁺ ions in situ to obtain the ENs (Figure S1). Scanning electron microscopy (SEM) images in Figure 1A show that both Zn-NCs and ENs present a nanocube morphology, confirming that Ru doping does not impair the structure of Zn-NC. Transmission electron microscopy (TEM) images further validate the nanocube morphology of both Zn-NCs and ENs with a similar particle size of 150 nm (Figure 1B). Similarly, the Ru clusters could be clearly detected on the surface of EN, and elemental mapping confirmed the existence of Zn and Ru in ENs (Figures 1C, S2). Figure 1D shows the X-ray diffraction (XRD) patterns of Zn-NCs and ENs; the Zn-NCs exhibit fine Zn-2-methylimidazole framework-assembled crystalline structures. The major framework structures were maintained after doping with Ru ions. Xray photoelectron spectroscopy (XPS) was used to investigate the composition and electronic structure of the EN nanoparticles. Figure 1E shows the XPS survey spectra in the presence of C, N, O, and Zn in the Zn-NCs and C, N, O, Zn, and Ru in the ENs, which is consistent with the TEM elemental mapping results (Figure 2C). The high-resolution Ru 3p spectrum (Figure 1F) exhibited characteristic peaks of the zerovalent Ru cluster with an apparent $3p_{1/2}$ peak at 484.47 eV along with a Ru 3p_{3/2} peak at 462.57 eV. Notably, the highresolution Zn 2p spectra confirm the similar Zn valence states in both ENs and Zn-NCs (Figure 1G). ^{28–30}

Hydrogen peroxide (H₂O₂) is an essential ROS agent and serves as the source of many other radical species in tendon injury. 5,9 CAT can decompose H₂O₂ into H₂O and O₂, which is a crucial kind of enzyme in biological redox equilibrium maintenance. 31,32 Consequently, we examined the CATmimetic activity of ENs by monitoring the scavenging of H_2O_2 and the generation of O_2 . ^{33–35} The ENs show a high H_2O_2 elimination rate with 90.9% decomposition of H_2O_2 in the first 5 min, whereas the Zn-NCs could not eliminate H₂O₂ (Figure 1H). Simultaneously, the evaluation of the generation of O₂ showed that ENs quickly and thoroughly decomposed H₂O₂ into O₂ and H₂O (Figure 11). The O₂ generation rate and H₂O₂ conversion rate both sustain the efficient CAT-mimetic ability of ENs (Figure S3, O₂ generation rate: 60.49 mg/L·min⁻¹ of EN; H₂O₂ conversion rate: 36.24 mmol/g_{cat}·min⁻¹ of EN). ENs exhibited a dose-dependent response in H₂O₂ scavenging and O_2 generation. At an extremely low concentration of 10 μ g/mL, ENs achieved a 91.2% decomposition ratio in 30 min and an O₂ generation rate of 40.98 mg/L in 1 min (Figures 1K,L, S3, and S4). Thus, the Ru doping endowed the nanoparticles with efficient H₂O₂ scavenging activity (Figure 1J). Moreover, we have confirmed that ENs can eliminate reactive nitrogen species

(Figure S5). Overall, we successfully constructed the EN biocatalyst with great CAT-mimetic ability for ROS-scavenging applications.

Construction and Analysis of ENEVs. The previous section validated that the EN biocatalyst exhibited efficient CAT-mimetic ability; therefore, we then constructed the ENEVs and fully characterized these nanohybrids. The preparation scheme of the ENEVs is presented in Figure 2A. BMSCs were selected as the source of EVs because of their established therapeutic benefits in musculoskeletal disorders. 18,19 The primary rat BMSCs were extracted, and the stem cell phenotype was identified with flow cytometry and cellular differentiation assays. As shown in Figure S6, the proportions of CD90- and CD44h-positive cells (MSC markers) were 99.9% and 80.9%, respectively, whereas the leukocyte marker CD45 was negatively expressed. Moreover, with stimulation by the induction medium, the BMSCs could differentiate into osteoblasts, chondrocytes, and adipocytes. The BMSC-EVs were then extracted via ultracentrifugation.³⁶ TEM imaging showed that the EVs exhibited a standard phospholipid bilayer structure (Figure 2B), and the nanoparticle tracking analysis (NTA) demonstrated that the average size of the EVs was 145.1 nm in diameter (Figure 2C).

According to recent studies, 37,38 the cloaking of EVs onto positive nanoparticles could be accomplished by co-incubating the two agents with shaking, whereupon ENs and EVs selfassembled through electrostatic interaction. TEM showed an approximate 20 nm thickness of the lipid membrane wrapped on the EN surface (Figures 2D,E and S7), which is similar to the surface morphology of the tumor exosome-cloaked nanoparticles.³⁹ The surface charge analysis showed that the ENs presented a positive surface charge, while the EVs were negatively charged (Figures 2F and S8). Additionally, the EVsspecific markers, including TSG-101, CD63, Alix, CD9, and CD81 (Figures 2G and S9), were presented in both EVs and the co-incubated products without the expression of calnexin, a protein located in the endoplasmic reticulum (Figure 2G). Moreover, Coomassie blue staining presented a protein profile of ENEVs similar to that of EVs (Figure S10). To verify the successful construction of ENEVs, we labeled the ENs with fluorescein isothiocyanate (FITC) and EVs with DiD (FITC-EN/DiD-EVs). After co-incubation and centrifugation, the precipitate was resuspended and then observed via confocal laser scanning microscopy (CLSM) (Figure 2H). The decoration rate was determined by calculating the percentage of yellow fluorescent particles (generated by the combination of red fluorescence from DiD-EVs and green fluorescence from FITC-ENs) to green fluorescent particles (bare FITC-EN particles). Approximately 79.12% (n = 3; SD \pm 10.87%) of the ENs were successfully coated by EVs (Figure 2I). Next, we evaluated the bound rate of the EVs by disclosing the change in the EVs concentration. As shown in Figure S11, the EVs concentration before co-incubation was $\sim 4.8 \times 10^{11}$ EVs/mL. After ENEV precipitation, the remaining concentration of EVs in the supernatant was $\sim 1.2 \times 10^{11}$ EVs/mL. Thus, 75.69 \pm 1.20% EVs (approximately 1.83×10^{11} EVs per mg EN) were coated onto the EN particles. Likewise, the ENEVs can sustainably release EVs, which displayed a Zn2+-release pattern similar to that of ENs, indicating that the release of EVs may be caused by the decomposition of ENs (Figures S12 and S13). These data indicate the successful construction of ENEVs and that the ENs retain the membrane integrity without interfering with the

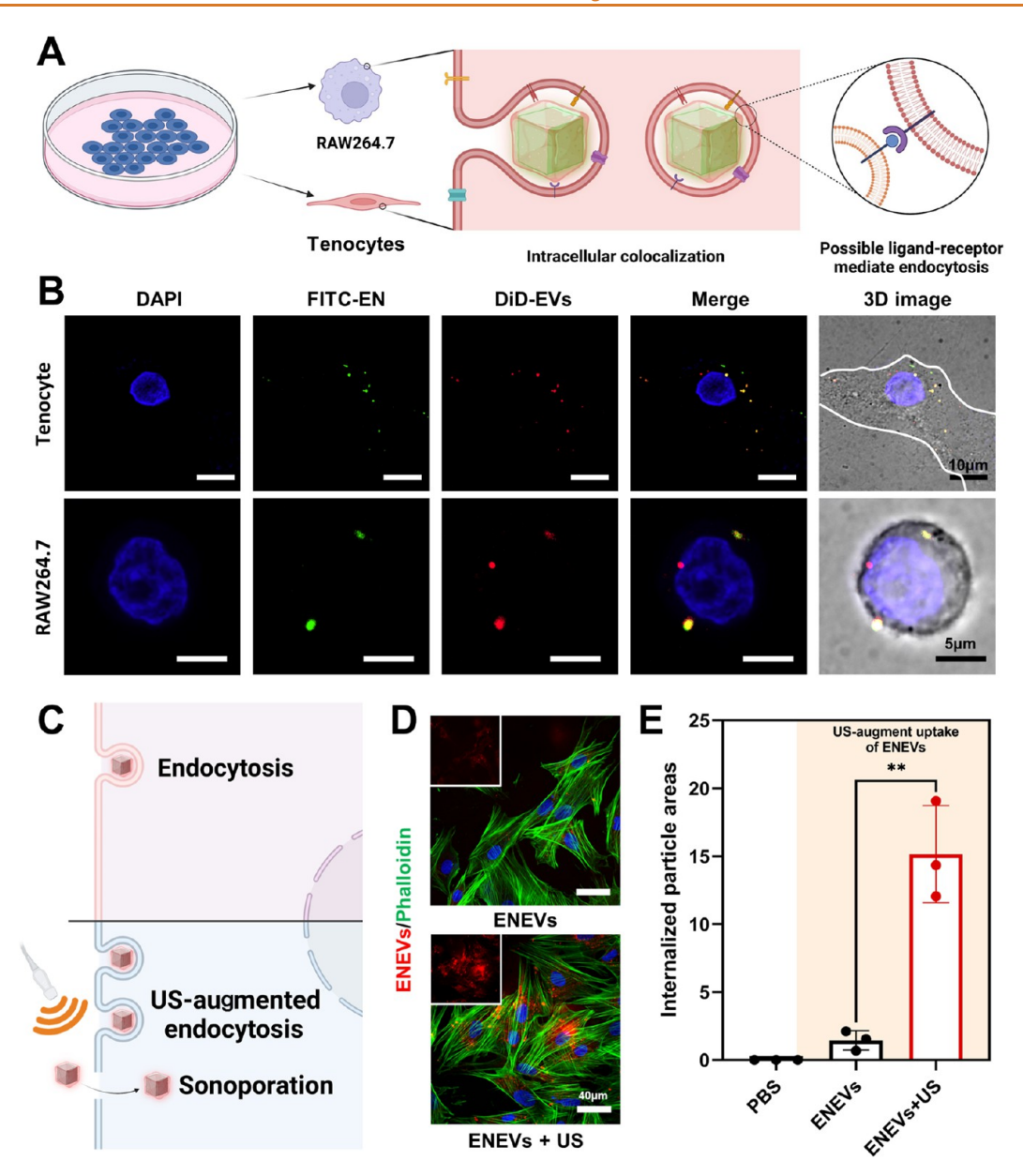


Figure 3. Cellular uptake of ENEVs. (A) Schematic of the investigation of cellular uptake of ENEVs and the possible mechanism. (B) CLSM images of tenocytes and RAW264.7 cells incubated with FITC-EN/DiD-EVs ($15 \mu g/mL$) for 4 h. Cell nuclei were stained with DAPI (blue). FITC-labeled ENs fluoresced green, and DiD-labeled EVs fluoresced red. (C) Schematic of the US-augmented cellular uptake mechanism. (D) Representative CLSM images of the EN/DiD-EVs uptake by tenocytes with US irradiation (1 MHz, 0.5 W/cm^2 , 1 min) applied to the ENEVs + US group 30 min after the addition of EN/DiD-EVs. Cell nuclei were stained with DAPI (blue), cytoskeletons were labeled with FITC-phalloidin (green), and EN/DiD-EVs were labeled with DiD (red). (E) Semiquantitative analysis of intracellular particle areas (n = 3 per group). Data are presented as mean \pm SD. Asterisks indicate p values; **p < 0.01.

cargo, which may provide better the rapeutic effects endowed by the EVs. $^{40-42}\,$

Biocompatibility and Cellular Uptake of ENEVs. Previous studies demonstrated that Zn-based frameworks could promote the proliferation of BMSCs owing to the release of Zn²⁺ ions, ⁴² and a gradual release of Zn²⁺ ions from Zn-NCs and ENs was also observed at room temperature in our study (Figure S13). Zn²⁺ ions can promote the proliferation of tenocytes and matrix reconstruction through upregulating COLII synthesis and downregulating COLIII deposition. ²⁶ Consequently, we examined the application potential of ENs in the promotion of tenocyte proliferation. First, our nanomaterials ($<30 \ \mu g/mL$) did not exhibit any toxicity after co-

incubation with tenocytes for 24 h (Figure S14). Then, the proliferation assay showed that the live cell ratios on day 5 increased 1.41- and 1.38-fold when stimulated by ENs at concentrations of 10 and 15 μ g/mL, respectively (Figure S15). Similar results were found in the Zn-NC group (Figure S16), indicating that the acceleration of tenocyte proliferation may be attributed to Zn²⁺ released by the Zn-NCs and ENs.

Furthermore, the cellular uptake of ENEVs was evaluated. The uptake of EVs by cells mainly occurs through endocytosis. ⁴³ We incubated tenocytes and RAW264.7 cells (a murine $M\varphi$ cell line) with FITC-EN/DiD-EVs or DiD-EVs alone to explore the uptake mode of ENEVs (Figure 3A). CLSM imaging proved that the FITC-EN/DiD-EVs were internalized by tenocytes and

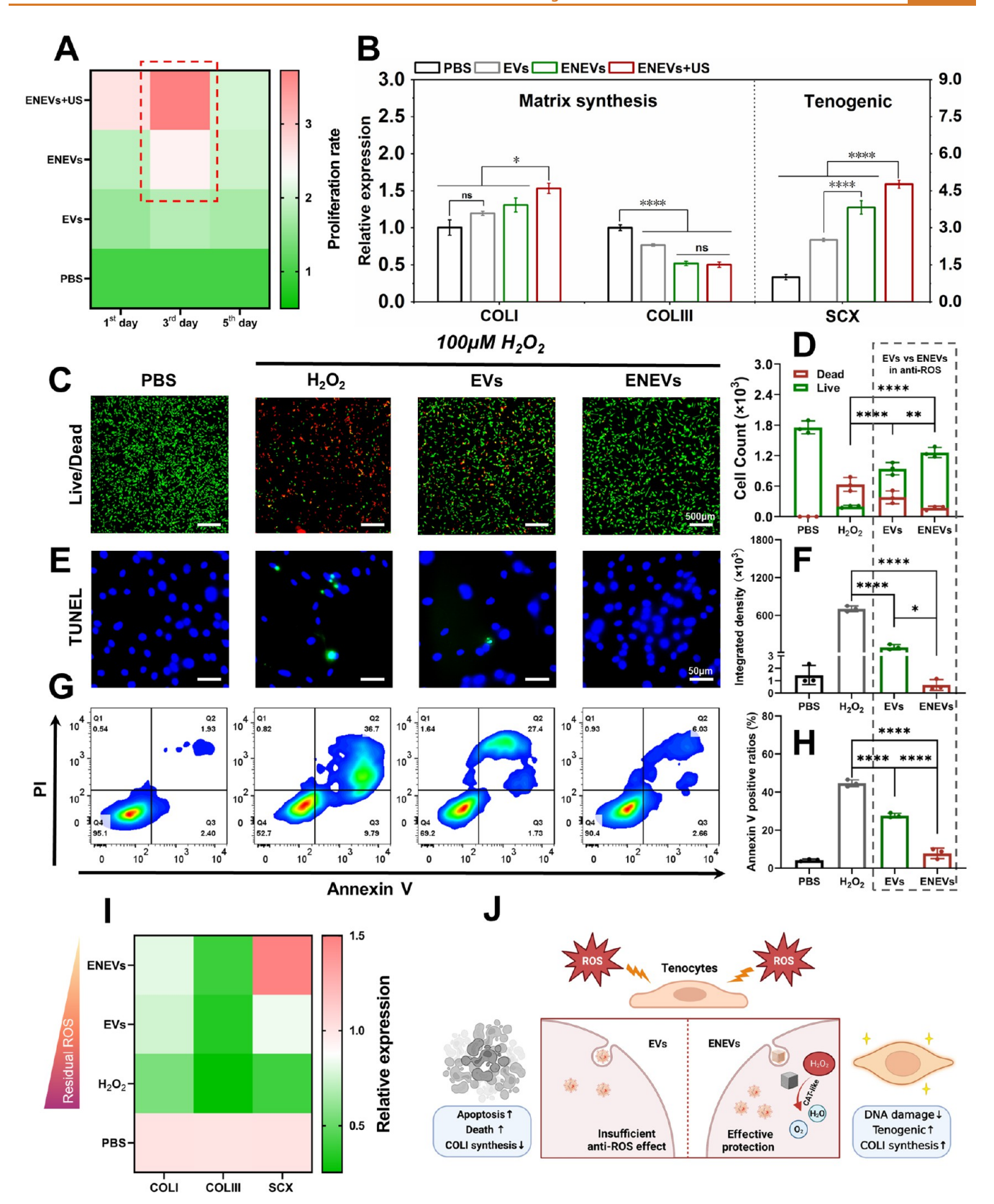


Figure 4. ENEVs promote the regeneration of tenocytes and protect them from ROS attacks. (A) Heat map represents the semiquantitative results of the Calcein-AM staining of tenocytes incubated with different agents for 1, 3, and 5 days. Data are presented in the form of the live cell number of the indicated group divided by the live cell number of the PBS group. (B) Expression of COLI, COLIII, and SCX mRNA in tenocytes after the indicated stimulation for 24 h measured via RT-qPCR. (C) Representative Live/Dead staining (green: live, red: dead) and (D) corresponding quantitative analysis of the cell counts after the indicated stimulation for 24 h. (E) TUNEL staining (green: TUNEL positive, blue: cell nuclei) of tenocytes and (F) the corresponding semiquantitative analysis of the integrated density of green fluorescence after the

Figure 4. continued

indicated stimulation for 24 h. (G) Annexin V/PI-labeled flow cytometry assay of tenocytes and (H) the corresponding quantitative analysis of the Annexin V-positive cell ratios after the indicated stimulation for 24 h. (I) Heat map represents the expression of COLI, COLIII, and SCX mRNA in tenocytes under H_2O_2 stimulation and different rescue treatments. (J) Schematic of the possible mechanism of ENEVs in defending tenocytes from ROS attack. In the above experiments, n = 3 per group. Data are presented as mean \pm SD. Asterisks indicate p values; *p < 0.05, ***p < 0.01, ****p < 0.0001, and ns represents no significant difference.

RAW264.7 since the green and red fluorescence were ideally colocalized (Figure 3B), while only red fluorescence was present intracellularly in the DiD-EVs group (Figure S17). This result provided support to prove the simultaneous delivery of both the ENs and the coated EVs. Currently, the mechanisms that regulate the cellular uptake of EVs are to be determined. Mostly, they involve protein interactions that facilitate subsequent endocytosis. Many EVs proteins can interact with membrane receptors on target cells. 43 As depicted in Figures 2G and S9, we found that EVs expressed the surface receptors CD81, CD63, and CD9, which are both EVs markers and the adhesion molecules that facilitate EVs and ENEVs incorporation into cells. 43,44 This membrane protein interaction process can increase the contact between EVs and the target cells to support the effective delivery of the ENEVs. Medical US has been applied as a drug delivery facilitator for decades because this is noninvasive and has strong tissue penetrative and focusing abilities.⁴⁵ The sonoporation effect of US can increase the permeability of cell membrane and augment the endocytosis process, thus enhancing cellular uptake (Figure 3C). 46-49 Here, we used EN/DiD-EVs to analyze US-augmented endocytosis. After a 4-h incubation, the tenocytes in the US-irradiated group presented a significantly higher amount of intracellular EN/ DiD-EVs with an increased endocytic ratio (15.15% of US irradiation group vs 1.45% of the non-US group. Figures 3D,E and S18). Collectively, our results show that the ENEVs are instantly delivered and that US enhances the cellular uptake process, which may improve the therapeutic effects.

Matrix Reconstruction and Anti-ROS Protection **Effects.** The tenocyte viability is the foundation of tendon regeneration, and COLI rather than COLIII forms the superstructure of the newly formed tendon tissue. However, the ROS generation during tendon injury reduces the viability of tenocytes and results in less COLI synthesis, which consequently increases the COLIII/COLI ratio. 5,50 Therefore, we assessed the pro-regeneration and anti-ROS abilities of ENEVs on tenocytes. The proliferation assay results in Figures 4A and \$19 indicate that the EVs, ENEVs, and ENEVs + US groups exhibited more proliferation than that in the phosphate buffered saline (PBS) group. The effect of ENEVs was significantly greater than that of EVs, demonstrating a synergistic effect between ENs and EVs (ENs also boost tenocyte proliferation). Notably, the US-irradiated group produced an increased proliferation effect on days 1 and 3 (2.66- and 3.62-fold, respectively), which was also confirmed with a viability assay (Figure S20). No significant difference was observed in the proliferation rate on day 5 when compared with the ENEVs group (2.04- vs 1.98-fold; p = 0.9982). This phenomenon may result from the US-enhanced cellular uptake of the ENEVs, which more strongly promotes proliferation to induce a quicker entrance of tenocytes into their logarithmic growth phase. Furthermore, contact inhibition caused by overcrowded cells occurred on day 5, which prevented the excessive proliferation of tenocytes.

We then used RT-qPCR (Figures 4B and S21) to show that EVs could slightly upregulate the expression of COLI mRNA expression but without a significant difference (1.20 vs 1.00; p =0.07). However, the expression level of COLI mRNA was significantly increased in the ENEVs group (1.31 vs 1.00; p =0.007) and was even higher under US irradiation (1.53 vs 1.00; p = 0.0002). Further, the expression level of COLIII mRNA was significantly downregulated in each treatment group. The ENEVs and ENEVs + US groups presented a higher suppressive effect on COLIII mRNA expression than that of the bare EVs group (0.52 vs 0.77; p < 0.0001). Additionally, the COLIII/ COLI ratios were prominently suppressed by ENEVs intervention, indicating a matrix reconstruction process (Figure S22). Scleraxis (SCX) is an important tenogenic marker and transcriptional activator of tenocytes whose expression is positively correlated to the formation of tendon tissue and the repair of tendon injury. Our results demonstrated that the expression of SCX mRNA was prominently increased in the EVs and ENEVs groups. The US-irradiation group also presented the highest SCX mRNA expression level. In summary, the USaugmented uptake of ENEVs was the most effective in inducing matrix reconstruction and tenogenic stimulation. Moreover, suppressing COLIII expression can prevent tendon adhesion and scar formation to benefit postoperative rehabilitation. These results suggest that US irradiation is essential for the quick action of ENEVs, which can prevent changes in collagen type during the initial phase of recovery from an acute tendon injury.

Stimulation with H₂O₂ is known to produce an oxidative stress environment that can simulate ROS accumulation in acute tendon injury. 8,52 Here, we investigated the protective effect of ENEVs on tenocytes against H_2O_2 . First, we determined that the induction of 100 μ M H₂O₂ for 3 h was appropriate for the *in vitro* ROS attack model, as the viability of tenocytes was impaired by approximately 50% (Figure S23). Next, the CCK-8 assay (Figure S24) and Live/Dead staining (Figures 4C,D and S25) were used to demonstrate that co-incubation of tenocytes with EVs presented partial rescue effects and that the ENEVs showed a superior result. DNA breakage is an important cellular damage caused by accumulated ROS. ^{53,54} As expected, TUNEL staining, which labels DNA fractures with green fluorescence, showed that DNA damage was found in the H₂O₂-treated groups and was barely observed in the EVs-treated group. Negative TUNEL staining was confirmed in the ENEVs group (Figures 4E,F and S25). Furthermore, the flow cytometry analysis of Annexin V/ PI-labeling showed that H₂O₂ caused an increase in the abundance of Annexin V-positive cells, which represent early and late apoptotic cells, and that this was suppressed by treatment with EVs but remained at a high level (Figures 4G,H and \$26). However, treatment with ENEVs presented an extraordinary protection effect compared to bare EVs (7.77% vs 27.65%; p < 0.0001).

Intriguingly, similar to previous reports, ^{21,55} we found that the BMSC-EVs could protect tenocytes from ROS attack and shared similar therapeutic effects with ENs. Furthermore, the ENEVs presented efficient synergic results contributed by both ENs and

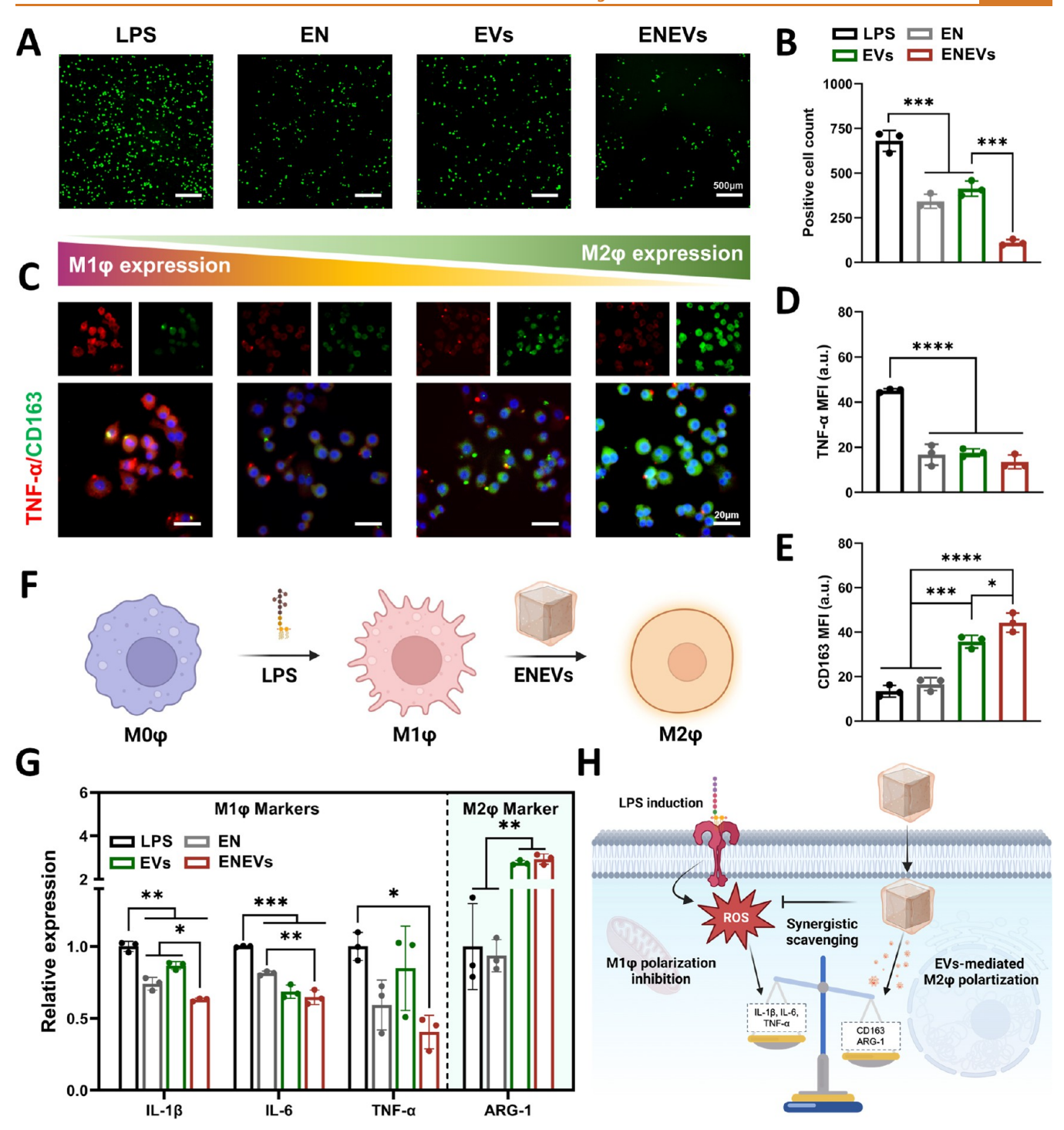


Figure 5. Intracellular ROS scavenging and $M\varphi$ s polarization regulation effects of ENEVs. (A) Representative images of intracellular ROS detected by DCFH-DA and (B) the quantitative analysis of the ROS-positive cell counts in the indicated groups. (C) Representative immunofluorescence images of TNF- α (red) and CD163 (green) staining of RAW264.7 cells after the indicated stimulation for 24 h. Nuclei were stained with DAPI (blue). (D) The semiquantitative analysis of the mean fluorescence intensity (MFI) of TNF- α and (E) CD163; au, indicates arbitrary units. (F) Schematic of the phenotype transition of M1 φ s toward M2 φ s triggered by ENEVs. (G) The expression of IL-1 β , IL-6, TNF- α , and ARG-1 mRNA of RAW264.7 cells after the indicated stimulation for 24 h was measured by RT-qPCR. (H) Schematic of the possible cellular mechanism of ENEVs in M φ s polarization regulation. In the above experiments, n=3 per group. Data are presented as mean \pm SD. Asterisks indicate p values; *p < 0.05, **p < 0.01, ****p < 0.001.

1

EVs. In addition, the RT-qPCR results (Figure 4I) revealed that the H_2O_2 decreased the expression of COLI mRNA and that this was partially reversed by ENEVs (0.55 vs 0.80; p = 0.034); meanwhile, the expression of SCX mRNA in ENEVs was even higher than that in the PBS group (without H_2O_2 stimulation,

1.49 vs 1.01; p = 0.045). The expression of COLIII mRNA remained unchanged after different treatments. Overall, our assessments of viability protection, anabolism maintenance, and tenogenic promotion suggested that the ENEVs can more

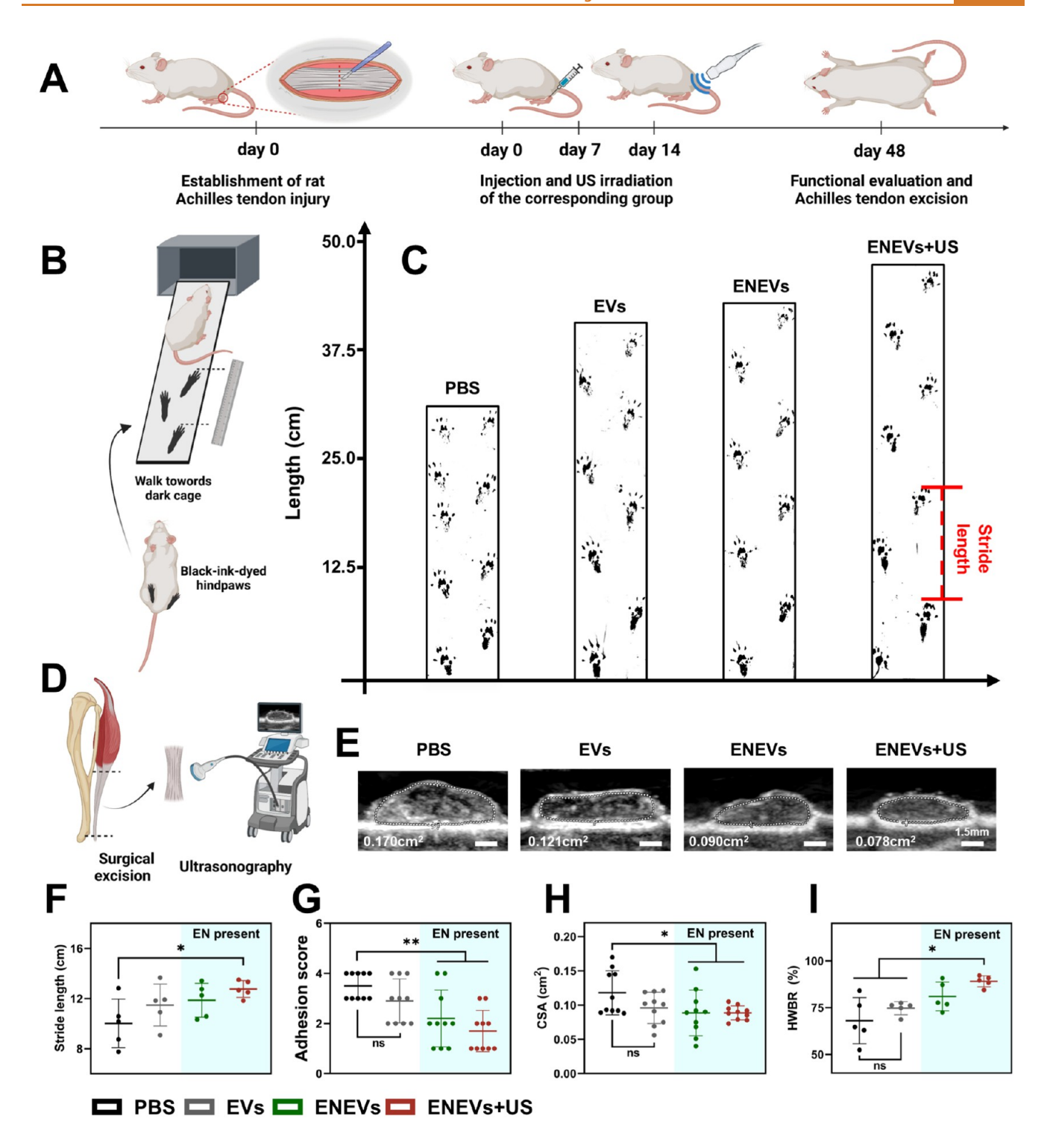


Figure 6. Morphology and biofunction analysis of the Achilles tendons at week 8 postoperatively. (A) Schematic of the establishment of the rat Achilles tendon injury model and treatment timeline. (B) Schematic of the gait analysis performance. (C) Representative gait analysis results of the indicated groups; the red line represents the stride length. (D) Schematic of ultrasonography assessment of the Achilles tendon cross-sectional area (CSA). (E) Representative ultrasonic images of the excisional tendons and the CSAs were measured. (F) Quantitative analysis of the stride length (n = 5 per group). (G) Adhesion score of the tendons (n = 10 per group). (H) Quantitative analysis of CSAs (n = 10 per group). (I) Quantitative comparison of the HWBRs (n = 5 per group). In the above experiments, data are presented as mean \pm SD. Asterisks indicate p values; *p < 0.05, **p < 0.01, and ns represents no significant difference.

effectively defend the tenocytes from ROS attack compared with EVs, as illustrated in Figure 4J.

The M φ s Polarization Regulation Effect of ENEVs. Lipopolysaccharide (LPS) can stimulate the M1 φ polarization

in a ROS-dependent manner and is a well-accepted proinflammatory *in vitro* model. ⁵⁶ Here, we used this model to evaluate the ROS-scavenging and $M\varphi$ s polarization regulation effects of ENEVs on RAW264.7 cells. Intracellular ROS was

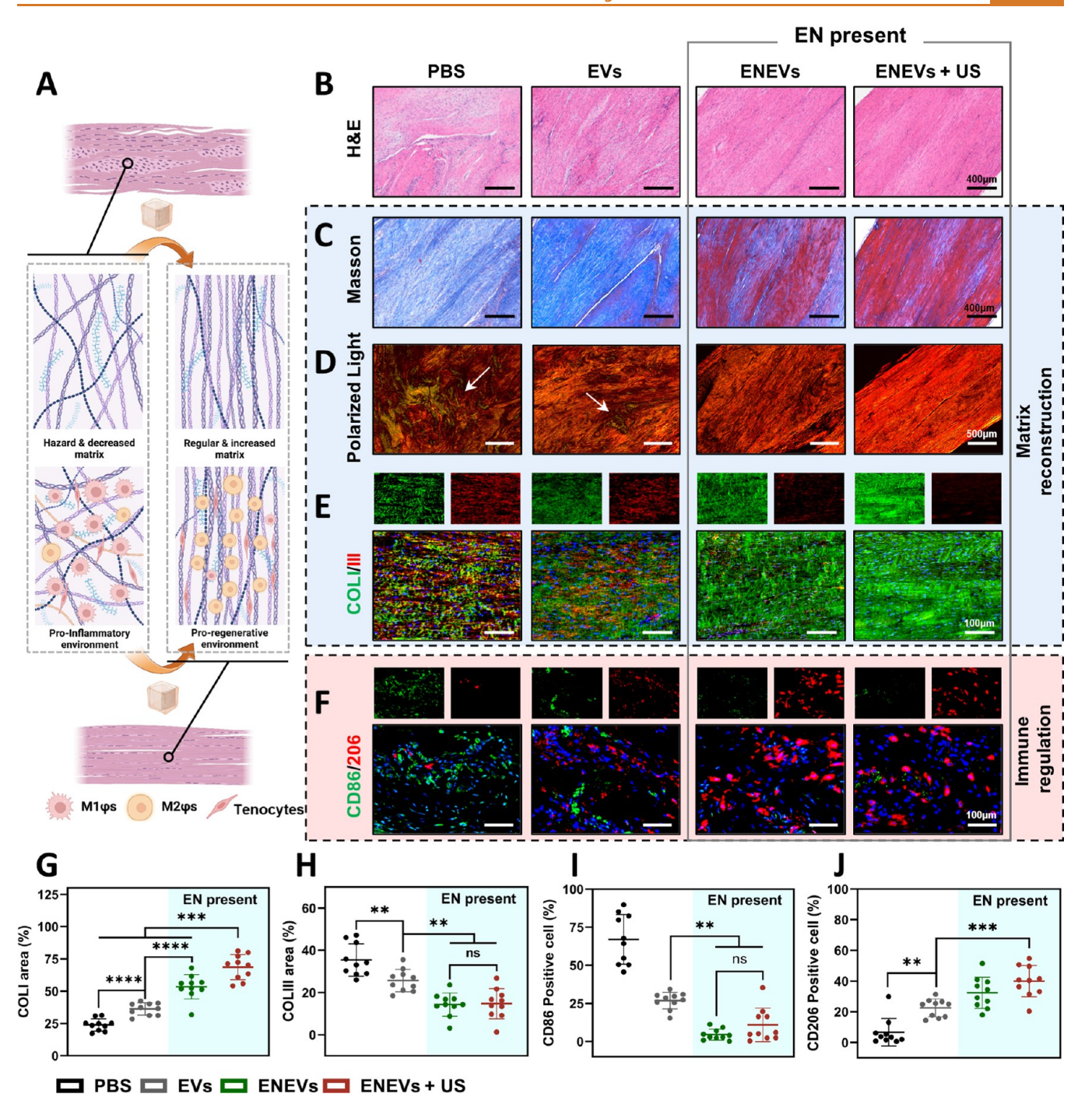


Figure 7. Histological assessments of the Achilles tendons at week 8. (A) Schematic of the histological therapeutic mechanisms of the ENEVs. (B) Representative images of H&E staining, (C) Masson staining, and (D) polarized light microscopy (stained with Sirius Red) of tendons from different groups. (E) Representative immunofluorescent images of COLI (green) and COLIII (red). (F) Representative immunofluorescent images of CD86- (green) and CD206- (red) positive cells. (G) Semiquantitative analysis of the COLI and (H) COLIII immunofluorescence images; results are presented as ratios for the positive area in each field of view. (I) Semiquantitative analysis of the CD86-positive cell ratios and (J) CD206-positive cell ratios in each field of view. In the above experiments, n = 10 per group. Data are presented as mean \pm SD. Asterisks indicate p values; **p < 0.001, ****p < 0.001, ****p < 0.0001, and ns represents no significant difference.

detected with 2',7'-dichlorofluorescein diacetate (DCFH-DA)⁵⁷ (Figure 5A and B), and LPS induction significantly triggered ROS accumulation in M φ s. Notably, EVs are reported to be effective in inhibiting LPS-induced ROS production^{58,59} and here presented a similar ROS-scavenging ability to that of ENs, with the ENEVs producing the most effective anti-ROS result. The polarization of M φ s was explored through immunofluorescence staining of TNF- α (the M1 φ s specific

marker) and CD163 (the M2 φ s specific marker; Figure 5C–E). TNF- α fluorescence signaling was intensely increased after LPS stimulation and could be efficiently suppressed by EN, EVs, and ENEVs. Although EN was robust in ROS scavenging and TNF- α inhibition, it negatively affected CD163 promotion. However, treatment with EVs produced a significant elevation in CD163 expression, and induction with ENEVs displayed superior promotion compared with EVs (44.02 vs 35.70; p = 0.048).

Thus, these data support the idea that ENEVs can regulate the polarization of $M\varphi s$ (Figure 5F).

RT-qPCR was performed to investigate the effect of ENEVs on the expression of inflammatory cytokines. Figure 5G shows that the treatment with ENEVs was the most effective in inhibiting the mRNA level of the pro-inflammatory cytokines, including that of IL-1 β , IL-6, and TNF- α . The expression of mRNA for ARG-1, another important M2 φ s specific marker, was significantly increased by EVs and ENEVs (Figure 5G). Overall, our results demonstrated that ENEVs could inhibit $M1\varphi$ s polarization through a synergistic ROS-scavenging ability and promote M2 φ s polarization in an EVs-dependent manner (Figure 5H). Our results show that ENEVs had a stronger therapeutic impact on reducing ROS level with greater suppression of inflammatory expression and promotion of $M2\varphi$ s polarization than that induced by bare EVs. This highlights that ENEVs provide a favorable pro-healing immune environment.

ENEVs Promoted Recovery of Achilles Tendon Injury. Given the great effects in tenocyte protection and M ϕ s polarization regulation, we assessed the in vivo therapeutic effects of ENEVs. The establishment of the rat Achilles tendon injury model and treatment timeline are presented in Figure 6A and Figure S27. After the injury, the inflammation stage spans several days and is then replaced by the proliferative stage. However, the remodeling stage begins 1–2 months after injury. Consequently, we chose a single dose immediately after surgery for inflammation inhibition. As for early tendon reconstruction therapy, we chose a single dose on days 7 and 14. The biodistribution and biodegradation of ENEVs were confirmed through in vivo fluorescence tests. We used IR783 to stain ENs and labeled EVs with DiR. The IR783-ENs, DiR-EVs, and IR783-EN/DiR-EVs were injected locally, and the distribution of these agents was observed with the IVIS Spectrum in vivo imaging system on days 1, 3, 5, and 7 after injection. As shown in Figure S28, the fluorescence intensity of ENs decreased rapidly, with only a marginal detection on day 5 and only 0.54% remaining on day 7. Conversely, EVs demonstrated prolonged retention, and the group with ENEVs exhibited an extended degradation period. These observations support the notion that EV cloaking can achieve a longer localized treatment effect. The US irradiation produced higher local retention on day 1 with a faster degradation rate, possibly attributed to the enhanced tissue penetration and cellular uptake of ENEVs, which augmented the initial local therapeutic effect. The organ distribution images acquired on day 7 indicate that the ENEVs mainly underwent renal clearance (Figure S29). Importantly, the fluorescence intensity in the kidneys from the ENEVs + US group was higher than that in the ENEVs group. This phenomenon may also result from the US-augmented cellular uptake and tissue penetration that led to enhanced ENEV utilization and clearance.

Next, the functional and morphological recovery of the Achilles tendons were assessed. The gait assessment was accomplished by measuring the stride length (Figure 6B). In week 8, the rats in the ENEVs + US group presented a significant recovery in stride length compared with that in the PBS group, whereas the other treatments did not show a significant difference (Figures 6C,F and S30). Next, the peritendinous adhesion degrees were evaluated through a visual examination according to an adhesion scoring system immediately after euthanasia. ^{48,60} Figure S31 shows that the PBS group displayed dense adhesion tissues that impaired the separation of the

tendon from the surrounding tissues. Less adhesion was found in the EVs group, whereas significantly less adhesion was found in the ENEVs and ENEVs + US groups (Figure 6G). This may be attributed to the inhibition of COLIII production by ENEVs, as this is the main matrix component in the adhesion and scar tissue. 61,62 One re-rupture at the left hindlimb of a rat in the PBS group was found on day 28 postoperatively (Figure S32). The cross-sectional areas (CSAs) of the separated tendon were visualized through ultrasonography (Figure 6D). As shown in Figure 6E and H, except for the EVs-treated group, the ENEVs and ENEVs + US groups all presented a significant decrease in CSAs compared to that in the PBS group. Treatment with the bare ENs also decreased the CSAs (Figure S33). As reported in an earlier study, 61 this phenomenon of deceased CSA may result from less scar formation and reduced deposition of COLIII, which was irregularly organized. Finally, the hindlimb weightbearing ratios (HWBRs) were calculated using an incapacitance meter (static weight bearing test) (Figure S34). Previous research demonstrated that rats with poorly recovered Achilles tendons might have lower HWBRs than rats with well-recovered tendons. 63 Surprisingly, we found that the HWBR was significantly increased in the ENEVs + US group, which indicated a good functional recovery of the Achilles tendons (Figures 6I and S34). This result may also be caused by the decreased local pain at the surgical sites of the rats in the ENEVs + US group, which could be attributed to the anti-inflammation effect of ENEVs. These results suggested that ENEVs with US irradiation can restore the morphology of Achilles tendons with less adhesion and scar formation because of the inhibited COLIII deposition. Furthermore, the assessment of the gait and the HWBR also suggested a functional recovery after treatment with ENEVs + US.

Figure 7A shows the histological therapeutic mechanism of the ENEVs. Hematoxylin and eosin (H&E) staining in the PBS group demonstrated that inflammatory cell infiltration was present in the intratendinous scar tissue (Figure 7B), accompanied by severe angiogenesis (Figure S35). The tendons in the PBS group also presented significant ectopic ossification and adipocyte infiltration (Figure S35), which represent poor histological recovery. Masson staining (Figures 7C and S36) demonstrated that collagen fibers in the PBS group were irregularly distributed with decreased density. Treatment with EVs induced partial restoration, and ENEVs treatment presented significantly higher effects compared with bare EVs. Notably, the combination of ENEVs with US irradiation induced an ideal degree of regeneration, as indicated by the dense, regular, and uniform alignment of the collagen fibers and the slender morphology of tenocytes. The polarized light microscopy results confirmed that a large number of green fibers (white arrow), which represent COLIII, were present in the scar tissues in the PBS group and were relieved by treatment with EVs (Figure 7D). No COLIII fibers could be observed in the ENEVs and ENEVs + US groups. Moreover, a distinct increase in the density of yellow-red fibers, which represents COLI, was confirmed in the ENEVs + US group.

The immunofluorescence staining images for COLI and COLIII are shown in Figure 7E. Our semiquantitative analysis confirmed that ENEVs have greater therapeutic effects in suppressing COLIII deposition and promoting COLI synthesis than that by EVs, and ENEVs + US produced the most effective COLI restoration (Figures 7G,H and S37). The expression of tenogenic marker (SCX) was promoted by ENEVs treatment, with or without US irradiation, indicating the high-level

maintenance of tenogenesis (Figure S38). The in vivo immune regulation effects were evidenced by immunofluorescence staining of CD86 (green, M1 φ s) and CD206 (red, M2 φ s) positive cells (Figures 7F and S39). The quantitative comparison demonstrates that a dramatic increase in the abundance of CD86-positive cells was found in the PBS group (Figures 7I, J and S39) and was mainly located in and near the intratendinous scar tissues, suggesting the activation of inflammatory responses. The intervention with ENEVs nanohybrids produced a significantly lower level of CD86-positive cell ratios than that produced by EVs. Importantly, The CD206positive cells were the dominating M φ s phenotype in the ENEVs and ENEVs + US groups. These results indicate the transformation of the tendon immune microenvironment from pro-inflammatory to pro-resolving was triggered by the immune regulatory effect of ENEVs. Finally, the biocompatibility of ENEVs was confirmed through H&E staining of organs and a hemolytic test that showed no pathological changes were present (Figure S40) and that hemolytic ratios were <5% (Figure S41). Overall, we conclude that the ENEVs nanohybrids can successfully reconstruct the matrix components and regulate the immune microenvironments during the recovery phase of tendon injury. The inhibition of COLIII deposition and promotion of COLI synthesis by ENEVs provide a great antiadhesion effect and aid in restoring tendon morphology and histological structure. In addition, the M2 φ -dominating immune environment provides stronger regeneration clues to tenocytes, thus further enhancing tendon regeneration.

CONCLUSION

Our study demonstrated that ENEVs could serve as an efficient multifaceted biocatalysts for US-augmented tendon regeneration and significantly promoted matrix reconstruction and immune microenvironment regulation. We systematically investigated the treatment merits and therapeutic effects of ENEVs to demonstrate the following advantages: efficient CATmimetic ability to scavenge ROS in the injured tissue, sustainable Zn²⁺ ion release, US-augmented cellular uptake ability, and extracellular vesicle-induced immunoregulation. Our study confirmed that ENEVs could promote tenocyte proliferation and COLI synthesis at an early stage by protecting tenocytes from ROS attack. Meanwhile, this report also validates that the ENEVs can efficiently reverse adverse immune responses by mediating the polarization of M φ from M1 φ to $M2\varphi$. Furthermore, by using a rat Achilles tendon defect model, we validated that the ENEVs can enhance functional recovery, restore tendon morphology, promote matrix reconstruction, suppress intratendinous scar formation, and inhibit peritendinous adhesion, especially with the assistance of US treatments. Therefore, we consider that this report describes an efficient nanomedicine for US-augmented biocatalytic tendon regeneration with significantly improved healing outcomes that could promote the development of multifaceted artificial biocatalysts to substitute current medicines for synergetic tissue regenerative therapies in diverse diseases.

METHODS

Preparation of Extracellular Vesicle-Cloaked Enzymatic Nanohybrid. First, 362 mg of $Zn(NO_3)_2\cdot 6H_2O$ and 10 mg of CTAB were dissolved in 18 mL of deionized water, and 5.65 g of 2-methylimidazole was dissolved in 82 mL of deionized water. The above two solutions were thoroughly mixed and then stirred for 1 h under room temperature. After centrifuging under 10000g for 10 min, the

precipitates were collected and washed with 50% ethanol three times. Then the precipitates were dried at room temperature to obtain the Zn-2-methylimidazole frameworks with nanocube morphology (Zn-based nanocube, Zn-NC). Next, 33.7 mg of RuCl₃·xH₂O was dissolved in 25 mL of deionized water, and 300 mg of Zn-NC was added with ultrasonic dispersion. Then 2 mL of 1 M NaBH₄ was added dropwise, and the mixture was allowed to react for 30 min. After centrifuging and washing with ethanol three times, the enzymatic nanocube (EN, Zn-NC with Ru cluster doping) is obtained. After drying in an oven at 60 °C for 24 h, both Zn-NC and EN were collected for further assessments.

The BMSC-EVs were isolated with ultracentrifuge methods. Briefly, the supernatant of primary cultured BMSCs was collected following 300g, 10 min, 4 °C, and another 3000g, 15 min, 4 °C centrifugation for separating the cells and debris. Then the supernatant was collected in 38.5 mL, Ultra-clear centrifuge tubes (344058, Beckman) following 120000g, 4 h, 4 °C centrifugation using an OPTIMA XPN-100 ultracentrifuge (Beckman) and resuspended with PBS. For the construction of ENEVs, 1 mg of EN was dissolved in 500 μL of BMSC-EVs cloaking solution with a concentration of $(4.0-5.0)\times 10^{11}$ EVs/mL. Then the tubes were placed on the rotary mixer for overnight co-incubation at 4 °C. Then, after centrifuging at 10000g for 5 min, the ENEVs were resuspended using sterile PBS.

ASSOCIATED CONTENT

Supporting Information

The Supporting Information is available free of charge at https://pubs.acs.org/doi/10.1021/acsnano.3c00911.

Discussions of materials and methods and experimental details, schematic synthesis process, elemental mapping, O₂ production rate, and H₂O₂ convention rate, digital photograph of the O₂ generation and DPPH scavenging analysis; identification of rat BMSCs, schematic of possible electrostatic self-assembly process of the ENEVs, TEM of ENEVs, immunoblotting analysis of EV markers, Coomassie blue staining, EV coating efficiency, EV release curve, and Zn²⁺ release profile; biocompatibility and proliferation analysis of ENs and Zn-NCs, CLSM images of ENEV uptake, Calcein-AM staining, viability assay of ENEVs, expression of COLI, COLIII, and SCX mRNA in tenocytes after EN stimulation, expression of COLIII compared with that of COLI (COLIII/COLI), scanning of H₂O₂ incubation concentration, viability analysis of tenocytes with different treated groups, live/dead and TUNEL staining of tenocytes treated with Zn-NCs or ENs under H₂O₂ stimulation, Annexin V/PI-labeled flow cytometry analysis of tenocytes after treatment with ENs under H₂O₂ stimulation; surgical reconstruction of Achilles tendon, in vivo fluorescence images, gait analysis results of sham, PBS, and EN groups, tendon adhesion visual examination and scoring, ultrasonography of sham, PBS, and EN groups, HWBR measurement of the PBS and EN groups, H&E staining of the intratendinous pathological changes; H&E staining, Masson staining, polarized light observation, and immunofluorescence images of sham and EN groups, immunofluorescence images of SCX expressions of different groups, H&E staining of the major organs, and the hemolysis test; table of RT-qPCR primer sequence (PDF)

AUTHOR INFORMATION

Corresponding Authors

Chong Cheng – College of Polymer Science and Engineering, State Key Laboratory of Polymer Materials Engineering,

- Sichuan University, Chengdu 610065, China; oorcid.org/0000-0002-6872-2240; Email: chong.cheng@scu.edu.cn
- Lang Ma Department of Ultrasound, National Clinical Research Center for Geriatrics, Med-X Center for Materials, West China Hospital, Sichuan University, Chengdu 610041, China; orcid.org/0000-0003-3741-1885; Email: malang1989@scu.edu.cn
- Li Qiu Department of Ultrasound, National Clinical Research Center for Geriatrics, Med-X Center for Materials, West China Hospital, Sichuan University, Chengdu 610041, China; orcid.org/0000-0003-2685-9799; Email: qiulihx@scu.edu.cn

Authors

- Xiao Rong Department of Ultrasound, National Clinical Research Center for Geriatrics, Med-X Center for Materials, West China Hospital, Sichuan University, Chengdu 610041, China; Orthopedic Research Institute, West China Hospital, Sichuan University, Chengdu 610041, China; orcid.org/ 0000-0002-3780-3902
- Yuanjiao Tang Department of Ultrasound, National Clinical Research Center for Geriatrics, Med-X Center for Materials, West China Hospital, Sichuan University, Chengdu 610041, China
- Sujiao Cao Department of Ultrasound, National Clinical Research Center for Geriatrics, Med-X Center for Materials, West China Hospital, Sichuan University, Chengdu 610041, China; College of Polymer Science and Engineering, State Key Laboratory of Polymer Materials Engineering, Sichuan University, Chengdu 610065, China; orcid.org/0000-0002-4251-7636
- Sutong Xiao Department of Ultrasound, National Clinical Research Center for Geriatrics, Med-X Center for Materials, West China Hospital, Sichuan University, Chengdu 610041, China; College of Polymer Science and Engineering, State Key Laboratory of Polymer Materials Engineering, Sichuan University, Chengdu 610065, China; ⊚ orcid.org/0000-0002-6050-8039
- Haonan Wang Orthopedic Research Institute, West China Hospital, Sichuan University, Chengdu 610041, China
- Bihui Zhu Department of Ultrasound, National Clinical Research Center for Geriatrics, Med-X Center for Materials, West China Hospital, Sichuan University, Chengdu 610041, China
- Songya Huang Department of Ultrasound, National Clinical Research Center for Geriatrics, Med-X Center for Materials, West China Hospital, Sichuan University, Chengdu 610041, China
- Mohsen Adeli Department of Organic Chemistry, Lorestan University, Khorramabad 6815144316, Iran
- Raul D. Rodriguez Tomsk Polytechnic University, 634034 Tomsk, Russia

Complete contact information is available at: https://pubs.acs.org/10.1021/acsnano.3c00911

Author Contributions

X.R. and Y.J.T. contributed equally to this work. Y.J.T. and S.J.C. synthesized all the materials. S.J.C. and S.T.X. assisted with the structural analysis. Y.J.T. and B.H.Z. performed the enzymemimetic evaluations together. X.R. and Y.J.T. performed most *in vitro* and *in vivo* experiments and the corresponding statistics analysis. H.N.W. and X.R. performed the isolation and identification of BMSCs and tenocytes, and H.N.W. designed

and performed the functional analysis of the rats. S.Y.H. and X.R. performed the extraction and identification of BMSC-EVs. X.R., Y.J.T., S.J.C., S.T.X., M.A., and B.H.Z. assisted with the figure production. X.R., Y.J.T., C.C., L.M., and L.Q. designed the experiments. X.R., Y.J.T., R.D.R., C.C., L.M., and L.Q. wrote and edited the manuscript.

Notes

The authors declare no competing financial interest.

ACKNOWLEDGMENTS

This work was financially supported by the National Key R&D Program of China (2019YFA0110600 and 2019YFA0110601), National Natural Science Foundation of China (Nos. 82001829, 82202187, 82272003, 82071938, and 52161145402), the Sichuan Science and Technology Program (Nos. 2022YFH0111, 2022YFH0112, 2023YFS0019, 2023YFH0008, and 2023YFH0031), the 1.3.5 Project for Disciplines of Excellence, West China Hospital, Sichuan University (No. ZYJC21047), Sichuan Provincial Health Commission Program (Nos. 21PJ011 and 21PJ012), and Fundamental Research Funds for the Central Universities (No. 2022SCU12051). We gratefully acknowledge Li Li, Fei Chen, and Chunjuan Bao of the Institute of Clinical Pathology, Sichuan University, for processing histological staining, and we also thank Li Chai, Yi Li, Xing Xu, and Li Zhou of the Core Facility of West China Hospital for the technical assistance.

REFERENCES

- (1) Seow, D.; Yasui, Y.; Calder, J. D. F.; Kennedy, J. G.; Pearce, C. J. Treatment of Acute Achilles Tendon Ruptures: A Systematic Review and Meta-Analysis of Complication Rates with Best- and Worst-Case Analyses for Rerupture Rates. *Am. J. Sports Med.* **2021**, *49* (13), 3728–3748
- (2) Attia, A. K.; Mahmoud, K.; d'Hooghe, P.; Bariteau, J.; Labib, S. A.; Myerson, M. S. Outcomes and Complications of Open Versus Minimally Invasive Repair of Acute Achilles Tendon Ruptures: A Systematic Review and Meta-Analysis of Randomized Controlled Trials. *Am. J. Sports Med.* 2023, *51* (3), 825–836.
- (3) Stavenuiter, X. J. R.; Lubberts, B.; Prince, R. M., 3rd; Johnson, A. H.; DiGiovanni, C. W.; Guss, D. Postoperative Complications Following Repair of Acute Achilles Tendon Rupture. *Foot Ankle Int.* **2019**, 40 (6), 679–686.
- (4) Millar, N. L.; Murrell, G. A.; McInnes, I. B. Inflammatory Mechanisms in Tendinopathy Towards Translation. *Nat. Rev. Rheumatol.* **2017**, *13* (2), 110–122.
- (5) Lui, P. P. Y.; Zhang, X.; Yao, S.; Sun, H.; Huang, C. Roles of Oxidative Stress in Acute Tendon Injury and Degenerative Tendinopathy-a Target for Intervention. *Int. J. Mol. Sci.* **2022**, 23 (7), 3571.
- (6) Li, P.; Zhou, H.; Tu, T.; Lu, H. Dynamic Exacerbation in Inflammation and Oxidative Stress During the Formation of Peritendinous Adhesion Resulted from Acute Tendon Injury. *J. Orthop. Surg. Res.* **2021**, *16* (1), 293.
- (7) Wang, F.; Murrell, G. A.; Wang, M. X. Oxidative Stress-Induced C-Jun N-Terminal Kinase (Jnk) Activation in Tendon Cells Upregulates Mmp1Mrna and Protein Expression. *J. Orthop. Res.* **2007**, 25 (3), 378–389.
- (8) Lee, Y. W.; Fu, S. C.; Yeung, M. Y.; Lau, C. M. L.; Chan, K. M.; Hung, L. K. Effects of Redox Modulation on Cell Proliferation, Viability, and Migration in Cultured Rat and Human Tendon Progenitor Cells. Oxid. Med. Cell. Longev. 2017, 2017, 8785042.
- (9) Wang, S. K.; Yao, Z. X.; Zhang, X. Y.; Li, J. H.; Huang, C.; Ouyang, Y. M.; Qian, Y.; Fan, C. Y. Energy-Supporting Enzyme-Mimic Nanoscaffold Facilitates Tendon Regeneration Based on a Mitochondrial Protection and Microenvironment Remodeling Strategy. *Adv. Sci.* **2022**, *9* (31), 2202542.

- (10) Freedman, B. R.; Kuttler, A.; Beckmann, N.; Nam, S.; Kent, D.; Schuleit, M.; Ramazani, F.; Accart, N.; Rock, A.; Li, J.; Kurz, M.; Fisch, A.; Ullrich, T.; Hast, M. W.; Tinguely, Y.; Weber, E.; Mooney, D. J. Enhanced Tendon Healing by a Tough Hydrogel with an Adhesive Side and High Drug-Loading Capacity. *Nat. Biomed. Eng.* **2022**, *6* (10), 1167–1179.
- (11) Sunwoo, J. Y.; Eliasberg, C. D.; Carballo, C. B.; Rodeo, S. A. The Role of the Macrophage in Tendinopathy and Tendon Healing. *J. Orthop. Res.* **2020**, 38 (8), 1666–1675.
- (12) Sugg, K. B.; Lubardic, J.; Gumucio, J. P.; Mendias, C. L. Changes in Macrophage Phenotype and Induction of Epithelial-to-Mesenchymal Transition Genes Following Acute Achilles Tenotomy and Repair. *J. Orthop. Res.* **2014**, 32 (7), 944–951.
- (13) Maffulli, N.; Barrass, V.; Ewen, S. W. Light Microscopic Histology of Achilles Tendon Ruptures. A Comparison with Unruptured Tendons. *Am. J. Sports Med.* **2000**, 28 (6), 857–863.
- (14) Maffulli, N.; Ewen, S. W.; Waterston, S. W.; Reaper, J.; Barrass, V. Tenocytes from Ruptured and Tendinopathic Achilles Tendons Produce Greater Quantities of Type Iii Collagen Than Tenocytes from Normal Achilles Tendons. An in Vitro Model of Human Tendon Healing. Am. J. Sports Med. 2000, 28 (4), 499–505.
- (15) Maeda, E.; Noguchi, H.; Tohyama, H.; Yasuda, K.; Hayashi, K. The Tensile Properties of Collagen Fascicles Harvested from Regenerated and Residual Tissues in the Patellar Tendon after Removal of the Central Third. *Biomed. Mater. Eng.* **2007**, *17* (2), 77–85.
- (16) Lee, W.; Kim, S. J.; Choi, C. H.; Choi, Y. R.; Chun, Y. M. Intra-Articular Injection of Steroids in the Early Postoperative Period Does Not Have an Adverse Effect on the Clinical Outcomes and the Re-Tear Rate after Arthroscopic Rotator Cuff Repair. *Knee Surg. Sports Traumatol. Arthrosc.* 2019, 27 (12), 3912–3919.
- (17) van Niel, G.; D'Angelo, G.; Raposo, G. Shedding Light on the Cell Biology of Extracellular Vesicles. *Nat. Rev. Mol. Cell Biol.* **2018**, *19* (4), 213–228.
- (18) Shi, Z.; Wang, Q.; Jiang, D. Extracellular Vesicles from Bone Marrow-Derived Multipotent Mesenchymal Stromal Cells Regulate Inflammation and Enhance Tendon Healing. *J. Transl. Med.* **2019**, *17* (1), 211.
- (19) Zhou, X.; Cao, H.; Guo, J.; Yuan, Y.; Ni, G. Effects of Bmsc-Derived Evs on Bone Metabolism. *Pharmaceutics* **2022**, *14* (5), 1012.
- (20) Gissi, C.; Radeghieri, A.; Antonetti Lamorgese Passeri, C.; Gallorini, M.; Calciano, L.; Oliva, F.; Veronesi, F.; Zendrini, A.; Cataldi, A.; Bergese, P.; Maffulli, N.; Berardi, A. C. Extracellular Vesicles from Rat-Bone-Marrow Mesenchymal Stromal/Stem Cells Improve Tendon Repair in Rat Achilles Tendon Injury Model in Dose-Dependent Manner: A Pilot Study. *PLoS One* **2020**, *15* (3), No. e0229914.
- (21) Li, X.; Su, Z.; Shen, K.; Wang, Q.; Xu, C.; Wang, F.; Zhang, Y.; Jiang, D. Eugenol-Preconditioned Mesenchymal Stem Cell-Derived Extracellular Vesicles Promote Antioxidant Capacity of Tendon Stem Cells in Vitro and in Vivo. *Oxid. Med. Cell. Longev.* **2022**, 2022, 3945195.
- (22) Chamberlain, C. S.; Kink, J. A.; Wildenauer, L. A.; McCaughey, M.; Henry, K.; Spiker, A. M.; Halanski, M. A.; Hematti, P.; Vanderby, R. Exosome-Educated Macrophages and Exosomes Differentially Improve Ligament Healing. *Stem Cells* **2021**, *39* (1), 55–61.
- (23) Chamberlain, C. S.; Clements, A. E. B.; Kink, J. A.; Choi, U.; Baer, G. S.; Halanski, M. A.; Hematti, P.; Vanderby, R. Extracellular Vesicle-Educated Macrophages Promote Early Achilles Tendon Healing. *Stem Cells* **2019**, *37* (5), 652–662.
- (24) Hu, Q.; Lyon, C. J.; Fletcher, J. K.; Tang, W.; Wan, M.; Hu, T. Y. Extracellular Vesicle Activities Regulating Macrophage- and Tissue-Mediated Injury and Repair Responses. *Acta Pharm. Sin. B* **2021**, *11* (6), 1493–1512.
- (25) Curtis, L. Nutritional Research May Be Useful in Treating Tendon Injuries. *Nutrition* **2016**, 32 (6), 617–619.
- (26) Yang, R.; Li, G.; Zhuang, C.; Yu, P.; Ye, T.; Zhang, Y.; Shang, P.; Huang, J.; Cai, M.; Wang, L.; Cui, W.; Deng, L. Gradient Bimetallic Ion-Based Hydrogels for Tissue Microstructure Reconstruction of Tendonto-Bone Insertion. *Sci. Adv.* **2021**, *7* (26), No. eabg3816.

- (27) Sun, Y.; Mu, S.; Xing, Z.; Guo, J.; Wu, Z.; Yu, F.; Bai, M.; Han, X.; Cheng, C.; Ye, L. Catalase-Mimetic Artificial Biocatalysts with Ru Catalytic Centers for Ros Elimination and Stem-Cell Protection. *Adv. Mater.* **2022**, 34 (46), 2206208.
- (28) Li, L.; Cao, S. J.; Wu, Z. H.; Guo, R. Q.; Xie, L.; Wang, L. Y.; Tang, Y. J.; Li, Q.; Luo, X. L.; Ma, L.; Cheng, C.; Qiu, L. Modulating Electron Transfer in Vanadium-Based Artificial Enzymes for Enhanced Ros-Catalysis and Disinfection. *Adv. Mater.* **2022**, *34* (17), 2108646.
- (29) Cao, S. J.; Zhao, Z. Y.; Zheng, Y. J.; Wu, Z. H.; Ma, T.; Zhu, B. H.; Yang, C. D.; Xiang, X.; Ma, L.; Han, X. L.; Wang, Y.; Guo, Q. Y.; Qiu, L.; Cheng, C. A Library of Ros-Catalytic Metalloenzyme Mimics with Atomic Metal Centers. *Adv. Mater.* **2022**, *34* (16), 2200255.
- (30) Ma, L.; Jiang, F. B.; Fan, X.; Wang, L. Y.; He, C.; Zhou, M.; Li, S.; Luo, H. R.; Cheng, C.; Qiu, L. Metal-Organic-Framework-Engineered Enzyme-Mimetic Catalysts. *Adv. Mater.* **2020**, *32* (49), 2003065.
- (31) Nandi, A.; Yan, L. J.; Jana, C. K.; Das, N. Role of Catalase in Oxidative Stress- and Age-Associated Degenerative Diseases. *Oxid. Med. Cell. Longev.* **2019**, 2019, 9613090.
- (32) Deng, Y.; Gao, Y.; Li, T.; Xiao, S.; Adeli, M.; Rodriguez, R. D.; Geng, W.; Chen, Q.; Cheng, C.; Zhao, C. Amorphizing Metal Selenides-Based Ros Biocatalysts at Surface Nanolayer toward Ultrafast Inflammatory Diabetic Wound Healing. ACS Nano 2023, 17 (3), 2943–2957.
- (33) Mu, S. D.; Deng, Y. T.; Xing, Z. Y.; Rong, X.; He, C.; Cao, S. J.; Ma, T.; Cheng, C.; Wang, Y. H. Ir Cluster-Anchored Mofs as Peroxidase-Mimetic Nanoreactors for Diagnosing Hydrogen Peroxide-Related Biomarkers. Acs Appl. Mater. Interfaces 2022, 14 (51), 56635—56643.
- (34) Long, Y. P.; Li, L.; Xu, T.; Wu, X. Z.; Gao, Y.; Huang, J. B.; He, C.; Ma, T.; Ma, L.; Cheng, C.; Zhao, C. S. Hedgehog Artificial Macrophage with Atomic-Catalytic Centers to Combat Drug-Resistant Bacteria. *Nat. Commun.* **2021**, *12* (1), 6143.
- (35) Du, F.; Liu, L.; Li, L.; Huang, J.; Wang, L.; Tang, Y.; Ke, B.; Song, L.; Cheng, C.; Ma, L.; Qiu, L. Conjugated Coordination Porphyrin-Based Nanozymes for Photo-/Sono-Augmented Biocatalytic and Homologous Tumor Treatments. ACS Appl. Mater. Interfaces 2021, 13 (35), 41485–41497.
- (36) Crescitelli, R.; Lässer, C.; Lötvall, J. Isolation and Characterization of Extracellular Vesicle Subpopulations from Tissues. *Nat. Protoc.* **2021**, *16* (3), 1548–1580.
- (37) Illes, B.; Hirschle, P.; Barnert, S.; Cauda, V.; Wuttke, S.; Engelke, H. Exosome-Coated Metal-Organic Framework Nanoparticles: An Efficient Drug Delivery Platform. *Chem. Mater.* **2017**, 29 (19), 8042–8046.
- (38) Kang, Y.; Xu, C.; Meng, L.; Dong, X.; Qi, M.; Jiang, D. Exosome-Functionalized Magnesium-Organic Framework-Based Scaffolds with Osteogenic, Angiogenic and Anti-Inflammatory Properties for Accelerated Bone Regeneration. *Bioact. Mater.* **2022**, *18*, 26–41.
- (39) Yong, T.; Zhang, X.; Bie, N.; Zhang, H.; Zhang, X.; Li, F.; Hakeem, A.; Hu, J.; Gan, L.; Santos, H. A.; Yang, X. Tumor Exosome-Based Nanoparticles Are Efficient Drug Carriers for Chemotherapy. *Nat. Commun.* **2019**, *10* (1), 3838.
- (40) Fathi, P.; Rao, L.; Chen, X. Extracellular Vesicle-Coated Nanoparticles. VIEW 2021, 2 (2), 20200187.
- (41) Cheng, G.; Li, W.; Ha, L.; Han, X.; Hao, S.; Wan, Y.; Wang, Z.; Dong, F.; Zou, X.; Mao, Y.; Zheng, S. Y. Self-Assembly of Extracellular Vesicle-Like Metal-Organic Framework Nanoparticles for Protection and Intracellular Delivery of Biofunctional Proteins. *J. Am. Chem. Soc.* **2018**, *140* (23), 7282–7291.
- (42) Gao, X.; Xue, Y.; Zhu, Z.; Chen, J.; Liu, Y.; Cheng, X.; Zhang, X.; Wang, J.; Pei, X.; Wan, Q. Nanoscale Zeolitic Imidazolate Framework-8 Activator of Canonical Mapk Signaling for Bone Repair. *ACS Appl. Mater. Interfaces* **2021**, *13* (1), 97–111.
- (43) Mulcahy, L. A.; Pink, R. C.; Carter, D. R. Routes and Mechanisms of Extracellular Vesicle Uptake. *J. Extracell Vesicles* **2014**, *3*, 24641.
- (44) Zhao, M.; Liu, S.; Wang, C.; Wang, Y.; Wan, M.; Liu, F.; Gong, M.; Yuan, Y.; Chen, Y.; Cheng, J.; Lu, Y.; Liu, J. Mesenchymal Stem Cell-Derived Extracellular Vesicles Attenuate Mitochondrial Damage

ACS Nano www.acsnano.org Article

- and Inflammation by Stabilizing Mitochondrial DNA. ACS Nano 2021, 15 (1), 1519–1538.
- (45) Deprez, J.; Lajoinie, G.; Engelen, Y.; De Smedt, S. C.; Lentacker, I. Opening Doors with Ultrasound and Microbubbles: Beating Biological Barriers to Promote Drug Delivery. *Adv. Drug Delivery Rev.* **2021**, *172*, 9–36.
- (46) Zeghimi, A.; Escoffre, J. M.; Bouakaz, A. Role of Endocytosis in Sonoporation-Mediated Membrane Permeabilization and Uptake of Small Molecules: A Electron Microscopy Study. *Phys. Biol.* **2015**, *12* (6), 066007.
- (47) Qin, P.; Han, T.; Yu, A. C. H.; Xu, L. Mechanistic Understanding the Bioeffects of Ultrasound-Driven Microbubbles to Enhance Macromolecule Delivery. *J. Controlled Release* **2018**, 272, 169–181.
- (48) Tang, Y.; Leng, Q.; Xiang, X.; Zhang, L.; Yang, Y.; Qiu, L. Use of Ultrasound-Targeted Microbubble Destruction to Transfect Igf-1 Cdna to Enhance the Regeneration of Rat Wounded Achilles Tendon in Vivo. *Gene Ther.* **2015**, 22 (8), 610–618.
- (49) Xiang, X.; Leng, Q.; Tang, Y.; Wang, L.; Huang, J.; Zhang, Y.; Qiu, L. Ultrasound-Targeted Microbubble Destruction Delivery of Insulin-Like Growth Factor 1 Cdna and Transforming Growth Factor Beta Short Hairpin Rna Enhances Tendon Regeneration and Inhibits Scar Formation in Vivo. Hum. Gene Ther. Clin. Dev. 2018, 29 (4), 198–213.
- (50) Sun, Y.; Mu, S.; Xing, Z.; Guo, J.; Wu, Z.; Yu, F.; Bai, M.; Han, X.; Cheng, C.; Ye, L. Catalase-Mimetic Artificial Biocatalysts with Ru Catalytic Centers for Ros Elimination and Stem-Cell Protection. *Adv. Mater.* **2022**, 34 (46), 2206208.
- (51) Ribatti, D. A Revisited Concept: Contact Inhibition of Growth. From Cell Biology to Malignancy. *Exp. Cell Res.* **2017**, 359 (1), 17–19.
- (52) Tian, Q.; Wang, W.; Cao, L.; Tian, X.; Tian, G.; Chen, M.; Ma, L.; Liu, X.; Yuan, Z.; Cheng, C.; Guo, Q. Multifaceted Catalytic Ros-Scavenging Via Electronic Modulated Metal Oxides for Regulating Stem Cells Fates. *Adv. Mater.* **2022**, *34* (43), 2207275.
- (53) Srinivas, U. S.; Tan, B. W. Q.; Vellayappan, B. A.; Jeyasekharan, A. D. Ros and the DNA Damage Response in Cancer. *Redox Biol.* **2019**, 25, 101084.
- (54) Du, F. X.; Liu, L. C.; Wu, Z. H.; Zhao, Z. Y.; Geng, W.; Zhu, B. H.; Ma, T.; Xiang, X.; Ma, L.; Cheng, C.; Qiu, L. Pd-Single-Atom Coordinated Biocatalysts for Chem-/Sono-/Photo-Trimodal Tumor Therapies. *Adv. Mater.* **2021**, 33 (29), 2101095.
- (55) Gu, S. S.; Kang, X. W.; Wang, J.; Guo, X. F.; Sun, H.; Jiang, L.; Zhang, J. S. Effects of Extracellular Vesicles from Mesenchymal Stem Cells on Oxygen-Glucose Deprivation/Reperfusion-Induced Neuronal Injury. *World J. Emerg. Med.* **2021**, *12* (1), 61–67.
- (56) Yang, B.; Yao, H.; Yang, J.; Chen, C.; Shi, J. Construction of a Two-Dimensional Artificial Antioxidase for Nanocatalytic Rheumatoid Arthritis Treatment. *Nat. Commun.* **2022**, *13* (1), 1988.
- (57) Wei, X.; Feng, Z.; Huang, J.; Xiang, X.; Du, F.; He, C.; Zhou, M.; Ma, L.; Cheng, C.; Qiu, L. Homology and Immune Checkpoint Dual-Targeted Sonocatalytic Nanoagents for Enhancing Sonodynamic Tumor Therapy. ACS Appl. Mater. Interfaces 2021, 13 (28), 32810–32822.
- (58) Shi, Z.; Wang, Q.; Zhang, Y.; Jiang, D. Extracellular Vesicles Produced by Bone Marrow Mesenchymal Stem Cells Attenuate Renal Fibrosis, in Part by Inhibiting the Rhoa/Rock Pathway, in a Uuo Rat Model. Stem Cell. Res. Ther. 2020, 11 (1), 253.
- (59) Cao, L.; Xu, H.; Wang, G.; Liu, M.; Tian, D.; Yuan, Z. Extracellular Vesicles Derived from Bone Marrow Mesenchymal Stem Cells Attenuate Dextran Sodium Sulfate-Induced Ulcerative Colitis by Promoting M2Macrophage Polarization. *Int. Immunopharmacol.* **2019**, 72, 264–274.
- (60) Ruan, H.; Liu, S.; Li, F.; Li, X.; Fan, C. Prevention of Tendon Adhesions by Erk2 Small Interfering Rnas. *Int. J. Mol. Sci.* **2013**, *14* (2), 4361–4371.
- (61) Millar, N. L.; Gilchrist, D. S.; Akbar, M.; Reilly, J. H.; Kerr, S. C.; Campbell, A. L.; Murrell, G. A. C.; Liew, F. Y.; Kurowska-Stolarska, M.; McInnes, I. B. Microrna29a Regulates II-33-Mediated Tissue Remodelling in Tendon Disease. *Nat. Commun.* **2015**, *6*, 6774.

- (62) Williams, I. F.; McCullagh, K. G.; Silver, I. A. The Distribution of Types I and Iii Collagen and Fibronectin in the Healing Equine Tendon. *Connect. Tissue Res.* **1984**, *12* (3–4), 211–227.
- (63) Wu, P. T.; Hsu, C. H.; Su, F. C.; Jou, I. M.; Chen, S. Y.; Wu, C. L.; Su, W. R.; Kuo, L. C. Dynamic Weight Bearing Analysis Is Effective for Evaluation of Tendinopathy Using a Customized Corridor with Multi-Directional Force Sensors in a Rat Model. *Sci. Rep.* **2017**, *7* (1), 8708.